

High-Temperature Photon-Noise-Limited Performance Terahertz Quantum-Well Photodetectors

J. Y. Jia, T. M. Wang, Y. H. Zhang, W. Z. Shen, and H. Schneider

Abstract—In this paper, we propose using a terahertz quantum-well photodetector (THz QWP) in combination with a terahertz source to realize a detection system with photon-noise limited performance (PLIP) at high temperatures. Systematical investigations on the high-temperature performances of THz QWPs, including required signal power density for PLIP, detectivity, and the signal-to-noise ratio, have been carried out by elaborating their dark current mechanism and photocurrent response both experimentally and theoretically. We also present the optimal doping concentration of THz QWPs designed for different peak wavelengths and the resulting optimum performance regarding the above three key parameters. Numerical results show that optimal designed QWP with peak response frequency of 5.5 THz is expected to achieve PLIP at 77 K at signal power density at 819 W/cm² and above. This work gives a precise description of PLIP performance of THz QWPs and will open ways for new applications for high-temperature detection in the THz regime.

Index Terms—High temperature, optimal design, photon-noise-limited, quantum-well photodetectors (QWPs), Terahertz (THz).

I. INTRODUCTION

THE rapid development of terahertz (THz) quantum cascade lasers (QCLs) as broadly tunable terahertz sources and their continuous performance improvements [1]–[6] impose urgent needs for high-performance THz detectors. Recently, THz quantum-well photodetectors (QWPs) have emerged as a promising candidate for compact detection systems in the THz region originating from the characteristics of intersubband

transition and unipolar transport. Compared with other THz detectors, for example, Si bolometers, thermal detector Golay cells, pyroelectric detectors made from LiTaO₃ crystals [7], nanometric FETs [8], or antenna-coupled field-effect transistors for THz imaging [9], THz QWPs show their special features in the detection performance: (i) THz QWPs are narrow band and enable wide wavelength coverage by adjusting the inter-subband transition energy. (ii) The intrinsic high speed due to the inherent short carrier lifetime helps THz QWPs to realize high-speed and high-frequency detection. (iii) The availability of a mature material and processing technology based on GaAs makes it possible to fabricate large-scale uniform and long-term stable THz QWPs. THz QWPs are designed as a natural extension of quantum well infrared (IR) photodetectors [10] and extensive research has been conducted to achieve better performance [11]–[14] after their first experimental demonstration [15]–[17]. However, THz QWPs still have a major limitation to their widespread use: they usually require cooling to low temperatures to realize background-noise-limited performance (BLIP) detection due to its lower barrier height in comparison with mid-IR QWP. The BLIP temperatures for THz QWPs are generally lower than 20 K [15], [17]. It is therefore crucial to develop optimized THz QWPs that can be operated at higher temperature. However, it seems not easy to increase the operating temperature of THz QWPs due to the resulting exponential increase of dark current and as a result, there is no systematical investigation that has been reported on high-temperature detection with THz QWPs. Fortunately, the breakthrough of THz QCL makes it possible to realize new applications (e.g., gas sensing and heterodyne detection) which require the combined use of THz QWP and QCL. By illumination with a QCL as the source or local oscillator in the THz region, the signal current of QWP could be made larger than the dark current at high operating temperature to realize photon-noise-limited performance (PLIP) detection. In this detection regime, the operation temperature can be increased above 77 K and even 100 K for high frequency QWPs in the THz region.

In this paper, we propose THz QWPs operated in PLIP regime in combination with a source such as THz QCL for high-temperature detection. In particular, we systematically investigate the performance of THz QWPs operated in PLIP regime both theoretically and experimentally by analyzing the dark current and photocurrent response. We also demonstrate the relation between the performances [e.g., required power density for PLIP,

Manuscript received March 28, 2015; revised June 07, 2015; accepted July 03, 2015. This work was supported in part by 863 Program of China under 2011AA010205, by the Natural Science Foundation of China under 91221201, 61234005, and 11074167, by the National Major Basic Research Projects 2011CB925603, and by the German Science Foundation under Grant DGG SCHN 1127/2.

J. Y. Jia and T. M. Wang are with the Department of Physics and Astronomy, Key Laboratory of Artificial Structures and Quantum Control (Ministry of Education), Shanghai Jiao Tong University, Shanghai 200240, China (email: jfyqsh@163.com).

Y. H. Zhang and W. Z. Shen are with the Department of Physics and Astronomy, Key Laboratory of Artificial Structures and Quantum Control (Ministry of Education), Shanghai Jiao Tong University, Shanghai 200240, China, and also with Collaborative Innovation Center of Advanced Microstructures, Nanjing University, Nanjing 210093, China (email: yuehzhang@sjtu.edu.cn; wzshen@sjtu.edu.cn).

H. Schneider is with the Institute of Ion-Beam Physics and Materials Research, Helmholtz-Zentrum Dresden-Rossendorf, Bautzner Landstr. 400, 01328 Dresden, Germany (e-mail: h.schneider@hzdr.de).

Color versions of one or more of the figures in this paper are available online at <http://ieeexplore.ieee.org>.

Digital Object Identifier 10.1109/TTHZ.2015.2453632

detectivity and signal-to-noise ratio (SNR)] and doping density in quantum wells (QWs). Moreover, the optimized design of THz QWPs for PLIP operation is presented and the performances of these optimally designed QWPs are also given and discussed in detail.

II. THEORY AND MODEL

A. Calculation of Band Structures

Unlike QWPs in the mid-IR region, THz QWPs have lower barrier height and thus lower transition energy. Additional physical interactions such as exchange correlation and depolarization should be taken into account in designing the band structure of THz QWPs [12], [18], [19]. For electrons in quantum well (QW) structures, the Schrödinger equation within the effective-mass approximation can be written as

$$\left\{ -\frac{\hbar^2}{2} \frac{\partial}{\partial z} \left[\frac{1}{m^*(z)} \frac{\partial}{\partial z} \right] + V_{QW}(z) + V_H(z) + V_{xc}(z) \right\} \varphi_{l,kz}(z) = \varepsilon_{l,kz} \varphi_{l,kz}(z) \quad (1)$$

Here z is the coordinate in the QW growth direction, \hbar is the reduced Planck constant, m^* is the electron effective mass, V_{QW} is the stepwise potential energy representing the periodic conduction band offset profile of the multiple QW, V_H is the Hartree potential energy obtained from Poisson's equation, V_{xc} is the exchange-correlation potential energy given by the local-density approximation (LDA) based on the density functional theory [20], [21], l is the miniband index and k_z is the wavevector in the z -direction, i.e., $k_z = m \cdot \pi / (L_p \cdot N_{QW})$, where $m = 0, 1, 2 \dots N_{QW}$. L_p is the period length of the multiple QW structure and equals the sum of well L_w and barrier L_b widths. N_{QW} is the number of QW periods. The boundary condition is taken as $\varphi_{l,kz}(0) = \varphi_{l,kz}(N_{QW}L_p)$. Concerning the minibands and wavevectors, we approximate the continuum by periodic states with respect to a large but finite N_{QW} . Here, both $N_{QW}=35$ for the test sample and $N_{QW}=30$ for the QWPs designed in Section IV give good approximations for the continuum. $\varphi_{l,kz}$ and $\varepsilon_{l,kz}$ correspond to the z -direction envelope function and the eigen-energy with miniband index l and wavevector k_z . Schrödinger equation and Poisson equation, along with the expression for exchange correlation form a closed set which should be solved self-consistently. In this paper, we numerically solve the above equations using a plane-wave expansion method and use $|(E_{F(i)} - E_{F(i-1)}) / E_{F(i)}| \leq 0.0001$ as the criteria to check the convergence. Here, $E_{F(i)}$ is the Fermi energy at the i th iterative step [19].

In the QWP structure, the number of electrons in the QWs with miniband index l and wavevector k_z is given by

$$N_{l,kz}(E_F) = \frac{m^*}{\pi \hbar^2} k_B T \ln \left[1 + \exp \left(\frac{E_F - \varepsilon_{l,kz}}{k_B T} \right) \right] \quad (2)$$

Through calculation, we find that the total electron densities in the lowest two subbands are orders of magnitude higher than the upper subbands. Therefore, we obtain the Fermi energy by solving

$$\sum_{l=1}^2 \sum_{kz} N_{l,kz}(E_F) = N_{2Ddope} N_{QW}. \quad (3)$$

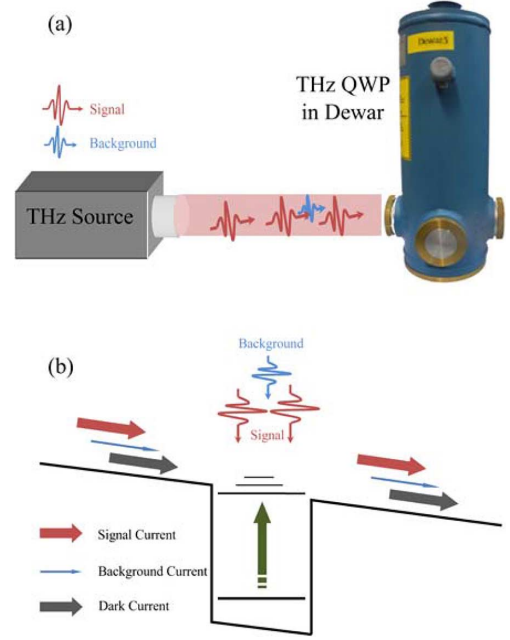


Fig. 1. Signal photocurrent and background photocurrent.

Here, N_{2Ddope} is the two-dimensional (2-D) doping concentration of each QW.

For a typical photodetector, the total current J_{total} originates from dark current generated by thermal activation, background current from the background radiation through the field-of-view (FOV) and signal current from the signal photon flux. Accordingly, J_{total} can, therefore, be expressed as a summation of the above three contributions:

$$J_{total} = J_{dark} + RP_B + RP_S. \quad (4)$$

Here, R is the detector responsivity, P_B and P_S are incident powers of background and signal radiation, respectively. Comparing the relative magnitudes of three contributions, the operating status of QWPs could be categorized into three performance regimes: dark current limited performance in which J_{dark} dominates, BLIP performance in which RP_B dominates and PLIP performance for which RP_S dominates. It is always desirable to operate QWPs under BLIP or PLIP regime for optimum sensitivity.

Fig. 1(a) is the schematic plot of combined use of THz QWP and THz source, which is expected to realize high-temperature detection. Fig. 1(b) shows the current transport mechanism of THz QWP under illumination. Even though high operating temperature results in large dark current, the signal photocurrent is larger and can become dominant (i.e., achieving PLIP condition) with a THz source. In this case, background photocurrent can always be neglected.

B. Dark Current

In standard theory of QWPs, three physical processes contribute to dark current, interwell tunneling which can be neglected due to the wide barrier, scattering-assisted tunneling (SAT) and thermionic emission (TE) [10], [22]. For QWPs in the THz region, the latter two processes are dominant accounting

for its low barrier height, operating temperature and bias. According to the emission-capture model, we give the dark current by [10]

$$J_{\text{dark}} = \frac{ev(F)\tau_c}{\tau_{\text{scatt}}} \int_{E_1}^{\infty} \frac{m}{\pi\hbar^2 L_p} T(E, F) \times \left[1 + \exp\left(\frac{E - E_F}{k_B T}\right) \right]^{-1} dE \quad (5)$$

The drift velocity is taken of the usual form $v(F) = \mu F / [1 + (\mu F / v_{\text{sat}})^2]^{1/2}$. v_{sat} and μ are the saturation velocity and low field mobility, respectively. τ_{scatt} is the scattering time of electrons from the ground state into the continuum state and τ_c is the capture time from the continuum back to the ground state. For QWPs in the mid-infrared region, the life time of excited electrons τ_c is mainly determined by optical phonon scattering and electron-electron scattering. For QWPs in the THz region (especially with the frequency < 7 THz) with transition energies less than the LO phonon energy of GaAs (36 meV), the phonon scattering would be weakened and electron-electron scattering will become dominant, which is expected to cause a reduced capture probability and thus an increased τ_c . Also, in this model, τ_c and τ_{scatt} just enter linearly and not in the exponent [see (5), (7a), (17) and (18)]. As a result, a small deviation in the estimation of τ_c and τ_c will have weak impact on the results of dark current and performances. Here, the scattering time is set as $\tau_{\text{scatt}} = 5$ ps and the life time of excited electrons is set as $\tau_c = 10$ ps [12]. $T(E, F)$ is the transmission coefficient calculated using the Wentzel–Kramers–Brillouin approximation as [10]

$$T(E, F) = 1, \quad \text{for } E \geq V \quad (6a)$$

$$T(E, F) = \exp\left[-2 \int_0^{z_c} dz \sqrt{2m_b(V - E - eFz)/\hbar}\right], \quad \text{for } E_1 \leq E < V \quad (6b)$$

where $V = V_b - eFL_w/2$ is the barrier height lowering by the applied electric field, $z_c = (V - E)/eF$ is defined as the classical tunneling point. E_1 is the ground state energy. For energy higher than the barrier, the dark current obtained corresponds to TE dark current which is always dominant for QWPs operating at high temperature and small bias. Thus, for high-temperature detection, (5) can be simplified to

$$J_{\text{dark}} = e \frac{\tau_c}{\tau_{\text{scatt}}} \frac{N_{2D}}{L_p} v \quad (7a)$$

$$N_{2D} = \frac{m}{\pi\hbar^2} k_B T \exp(-E_{\text{act}}/k_B T) \quad (7b)$$

where N_{2D} is the 2-D electron density only including electrons on the upper part (with energy greater than the barrier height) of the ground state subband. E_{act} is the activation energy defined as the difference between the barrier height and Fermi energy. For energy lower than the barrier, the dark current obtained corresponds to tunneling current including SAT (for $V - eFL_b \leq E < V$) and interwell tunneling (for $E_1 \leq E < V - eFL_b$).

C. Photoresponse

The photocurrent density generated by background radiation or monochromatic light (e.g., a laser) can be expressed as

$$J_{\text{photon}} = RP \quad (8)$$

P is the photon power density which can be categorized into P_B and P_S according to the source. The responsivity R is given by

$$R = \frac{e}{h\nu} \eta g_{\text{photo}} \quad (9)$$

where ν is the photon frequency. η is the peak absorption efficiency of the QWP in a 45 degree double pass geometry, which can be expressed as [10]

$$\eta = \frac{e^2 \hbar}{4\varepsilon_0 n_r m_w^* c} \frac{\sin^2 \theta}{\cos \theta} \sum_{kz} N_{l=1, kz}(E_F) f \frac{1}{\pi} \frac{\Gamma}{(h\nu - E_{21})^2 + \Gamma^2} \quad (10)$$

where ε_0 is the vacuum permittivity, the refractive index n_r is 3.3 for GaAs, $\theta = 45^\circ$ is the angle between THz radiation propagating direction and QW's growth direction, $\sum_{kz} N_{l=1, kz}(E_F)$ is the number of electrons in the ground state, E_{21} is the energy difference between the first excited state and the ground state. $f = 4\pi m_w^* v / \hbar \cdot |\langle \varphi_1 | z | \varphi_2 \rangle|^2$ is the oscillator strength, where φ_1 and φ_2 are the envelope functions in the ground and first excited states, respectively. $\Gamma = h\nu_c - h\nu_p$ is the Lorentzian linewidth constant, ν_c is the cutoff frequency defined as the frequency where η is 50% of the maximum, which approximately equals $1.1 \times \nu_p$ from the measured photocurrent spectra. $g_{\text{photo}} = p_e / N p_c$ is the photoconductive gain, where $p_e = 1 - p_c$ is the escape probability of photoexcited electrons from the emission zone and p_c is the capture probability for an electron (with energy larger than barrier height) traversing a well for photoconductive QWP.

D. Noise and Detectivity

As a photoconductive device, the conductivity of QWP increases with incident infrared power. Under normal circumstances, the photoconductivity of QWPs increases linearly with power, which means that the responsivity $R = J_{\text{photon}}/P_{\text{signal}}$ is constant. However, at high signal power [23], [24] nonlinear photoconductivity effects can take place, giving rise to a decrease of responsivity. This effect can be important, especially for gas sensing or heterodyne detection where high signal power is needed. This nonlinearity effect takes place at signal power much lower than that causing the saturation of intersubband absorption in QWs due to depletion of electrons in the ground state [25], [26]. For PLIP detection using THz QWPs, the nonlinearity effect has also been taken in account and discussed in detail.

In our calculation of the electric field distribution across the QWs, we apply the model in [24]. As indicated in Fig. 2(a), the total current J_{total} inside the QWP is the injected current at the first barrier adjacent to the emitter. At the remaining N_{QW} barriers of the structure, it consists of a photocurrent and a thermally induced dark current. In this model, F_2 is taken to be the average field across the remaining barriers as an approximation, which is reasonable both in the mid-IR [23], [24] and THz regions [27]. The total current J_{total} of the device with the incident signal power P_{signal} and the bias voltage $V_0 = L_p F_1 + N_{\text{QW}} L_p F_2$ can, therefore, be expressed as

$$J_{\text{total}}(V_0, P_{\text{signal}}) = J_{\text{inj}}(F_1) = J_{\text{dark}}(F_2) + P_{\text{signal}} R(F_2) \quad (11)$$

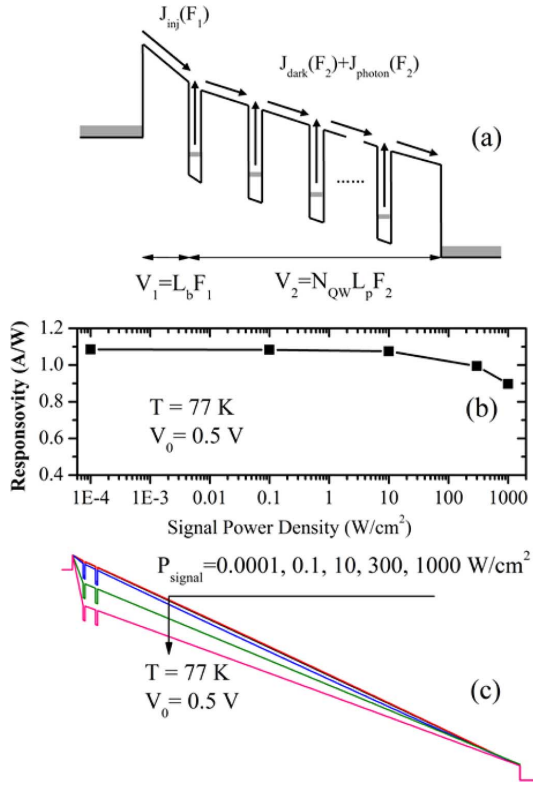


Fig. 2. (a) Schematic plot of conduction bandedge distribution of QWP under illumination. (b) Responsivity vs incident signal power of the test THz QWP sample (see detailed parameters in Section 3.1). $V_0 = 0.5$ V (1835.5 V/cm), $T = 77$ K, $P_{signal} = 0.0001, 0.1, 10, 300, 1000$ W/cm². (c) conduction band diagrams at 0.5 V, $T = 77$ K. For simplification, we only plot the first two QWs.

$J_{inj}(F_1)$ is the injected current from the contact [28], $J_{dark}(F_2)$ is the dark current including TE and SAT. $R(F_2)$ is the responsivity at local field F_2 , which could be thought as the signal responsivity for QWP samples with large number of QWs [24].

The results of the simulation according to (11) are shown in Fig. 2(b) and (c). The structure parameters of the tested QWP sample are presented in the Section III-A. The applied voltage is 0.5 V, i.e., average electric field of 1835.5 V/cm. The operation temperature used is 77 K, which corresponds to a PLIP power of 407 W/cm². As indicated in Fig. 2(b), the responsivity decreases slightly with the power. This can be explained by Fig. 3(c), which displays the band diagrams. An increase of excitation power results in redistribution of the potential. The electric field in the emitter barrier increases to provide an enhanced electron injection, while the electric field in the QWs of QWP decreases with power. Nevertheless, the responsivity does not decrease significantly (just by less than 17.3%) even under illumination densities of up to 1000 W/cm². This is because the photon-induced voltage drop near the emitter is much smaller than the applied voltage.

For practical applications, the dark current noise and the photocurrent noise often limit the ultimate detector performance in photoconductive QWPs. Due to the escape and the trapping processes controlling the dark current, the noise associated with dark current is generation-recombination (g-r) in nature. The

dark current noise is therefore given by the standard expression [29]

$$i_{n,dark}^2 = 4eg_{noise}J_{dark}\Delta f \quad (12)$$

where J_{dark} is the device dark current and $g_{noise} = 1/Np_c$ is the dark current noise gain. By definition, the noise gain g_{noise} is different from the photoconductive gain $g_{photo} = p_e/Np_c$. For THz QWPs, due to the bound-to-continuum transition case, the escape process of excited electrons is very efficient, i.e., once an electron is excited, it is already in the continuum. Also, the applied electric field could be increased to make the escape of electrons easier. In this case, an escape probability equal to unity is a good approximation for practical purposes and as a result, the photoconductive gain is taken as $g_{photo} = g_{noise} = 1/Np_c \approx \tau_c v/NL_p$.

The detector noise associated with the background or signal radiation is caused by fluctuations in the number of photons absorbed by a detector. For photoconductive QWPs, the noise current could be given by [29]

$$i_{n,photon}^2 = 4eg_{photo}J_{photon}\Delta f \quad (13)$$

The most important figure of merit is the detectivity D^* , which is given by

$$D^* = \frac{R\sqrt{A\Delta f}}{i_{n,total}} = \frac{g_{photo}\eta/h\nu}{\sqrt{4g_{noise}J_{dark}/e + 4g_{photo}J_{photon}/e}} \quad (14)$$

Generally, the SNR for QWPs can be expressed as

$$SNR = \frac{J_{photon}A}{\sqrt{4eg_{noise}J_{dark}\Delta f + 4eg_{photo}J_{photon}\Delta f}} \quad (15)$$

where A is the area of the THz QWP device. By definition, the PLIP regime is where the noise induced by J_{photon} in (14) and (15) is larger than the dark current noise.

III. EXPERIMENT AND DISCUSSION

A. Device Structure

The THz QWP device structure is designed and grown on a semi-insulating GaAs wafer by molecular beam epitaxy. The structure consists of 35 GaAs/Al_{0.04}Ga_{0.96} as QWs sandwiched between top (400 nm) and bottom (800 nm) contact layers, Si-doped to 10^{17} cm⁻³. The well width (12 nm), Al fraction (4%), doping density (10^{17} cm⁻³) and doping length (7 nm) are optimally designed such that only one energy state E_1 is bound in the QW and the excited state E_2 is close to resonance with the bottom of the barrier conduction band. The barrier width is designed thick enough to suppress the interwell tunneling dark current. Square mesa devices of various sizes (400×400 μm^2 , 800×800 μm^2 , and 1000×1000 μm^2) were fabricated using standard optical lithography and dry etching. The mesa top was covered completely by a metal coating (i.e., Pd/Ge/Ti/Pt/Au with 50/100/25/55/300 nm deposited by electron-beam evaporation), which increased the electric field at the semiconductor-metal interface. This configuration was necessary for the combined use of THz sources to provide PLIP regime considering the sample's large wavelength compared to

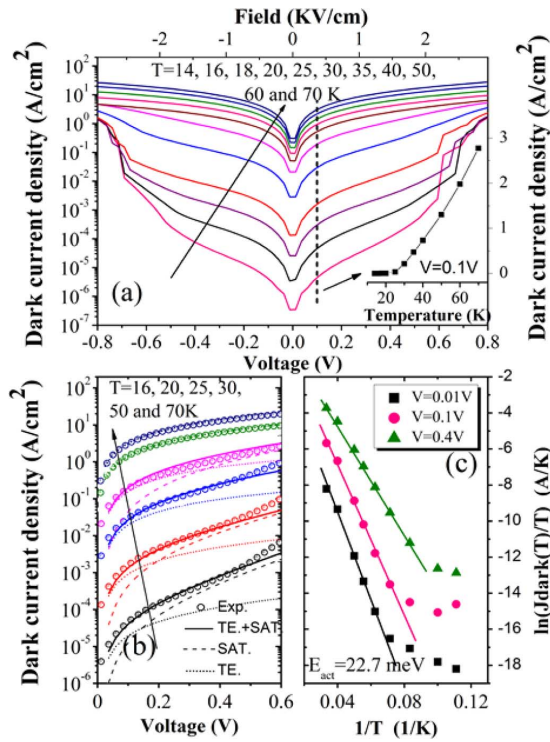


Fig. 3. (a) Measured dark current density of the test sample at different temperatures. The inset shows the dark current density at 0.1 V as a function of temperature. (b) Calculated and measured dark current at positive bias. Dotted, dashed, and solid lines represent TE, SAT and total dark current, respectively. (c) Arrhenius plots of the dark current at 0.01, 0.1 and 0.4 V. the activation energy estimated is 22.7 meV at 0.01 V.

the multiple QW thickness [30]. For optical characterization, samples were polished to give rise to a 45° facet and packaged into the standard double-pass back side illumination geometry with an internal incident angle of 45°. It should be noted that for some application such as real time imaging focal plane arrays, optical grating couplers are often used to realize normal incidence of the illumination [31]. Device characteristics were performed in a temperature-controlled helium cryostat.

B. Dark Current

Fig. 3(a) depicts the measured current–voltage (I – V) curves under dark condition for a set of temperatures from 14 to 70 K. As shown, the I – V curves show strong temperature dependence. We also give the dark current density at fixed bias (0.1 V) as a function of temperature as further described in the inset of Fig. 3(a). The dark current increases exponentially with temperature, which is consistent with previous investigations [15]–[17]. The bias of 0.1 V is chosen such that it does not appreciably alter the band structure when producing a measurable current through the THz QWP device. With increasing bias, the dark current density increases but shows an abrupt growth by nearly one order of magnitude when the bias reaches about 0.6 V. This remarkable transition occurs especially at low temperature since the extra electrons which are usually confined in QW can leak across the barriers due to an efficient ionization of the first QW, which has been discussed in detail by Guo *et al.* [27], Gomez *et al.* [32], and Delga *et al.* [33]. However, when it comes to high temperature, most of the

confined electrons escape into the continuum already by TE and SAT and the relative contribution by extra leakage due to ionization becomes negligible. The increasing trend of dark current density with bias is different at various temperatures from 14 to 70 K which is caused by the different dominated dark current mechanism.

To analyze the dark current mechanism at various temperatures in more detail, we show the calculated and measured dark current in Fig. 3(b). Dotted and dashed lines represent TE and SAT dark current, respectively. Solid lines indicate the total dark current. In our calculation, the interwell tunneling dark current was much smaller than TE and SAT, and thus could be neglected. As shown, at low temperature, both TE and SAT are significant contributions to the total dark current. At high bias, the SAT dark current can be several orders of magnitude higher than TE. As temperature rises, TE dark current plays more and more important roles in the total dark current. Especially, when the temperature reaches 50 and 70 K, the contribution of SAT can be ignored and TE becomes the dominant dark current. Hence, the dark current mechanism can be simplified into pure TE regime when THz QWPs are operated in the high-temperature region. So, for high-temperature PLIP detection, the dark current can be expressed as (7a) and (7b). For further analysis, (7a) and (7b) can be written as

$$\frac{J_{\text{dark}}}{T} \propto \exp\left(-\frac{E_{\text{act}}}{k_B T}\right). \quad (16)$$

By plotting the quantity $\ln(J_{\text{dark}}/T)$ against inverse temperature, we can deduce the value of E_{act} . Fig. 3(c) shows the plot of $\ln(J_{\text{dark}}/T)$ as the function of $1/T$ at three different biases, i.e., 0.01, 0.1 and 0.4 V. The straight lines give the E_{act} values of 22.7, 19.7 and 13.9 meV, respectively. Decreased E_{act} is observed with increasing of the bias, which is likely caused by the electric field induced barrier lowering effect and the remaining SAT process. The value of E_{act} obtained at 0.01 V where TE is considered to be dominant is in agreement with the activation energy obtained via the calculation of the band structure of THz QWPs (further details will be discussed later).

In summary, TE regime is dominant in total dark current when THz QWPs are operated at high temperature, which is demonstrated by theoretical calculation and the experimental measurement, also by the evaluation of E_{act} .

C. Photoresponse

Fig. 4 shows the response of our sample to THz radiation from a Bruker IFS 66S/V FTIR spectrometer which is optically coupled into the THz QWP active region using 45° facet. The device shows photodetector response up to 23 K (measured BLIP temperature is 16 K). From the response spectra, the peak response frequency is obtained at 226 cm⁻¹ (44 μm, 28 meV, 6.78 THz). The main dark region from 256 to 292 cm⁻¹ in the sample is due to GaAs optical phonon absorption in the substrate, other small features such as the dips at 312 and 338 cm⁻¹ are caused by two-phonon absorption. The dip at 362 cm⁻¹ in both samples corresponds to the AlAs-like phonon absorption.

The inset shows the band structure obtained from the Schrödinger equation (i.e., (1) taking into account the Hartree potential and the exchange-correlation potential. The transition

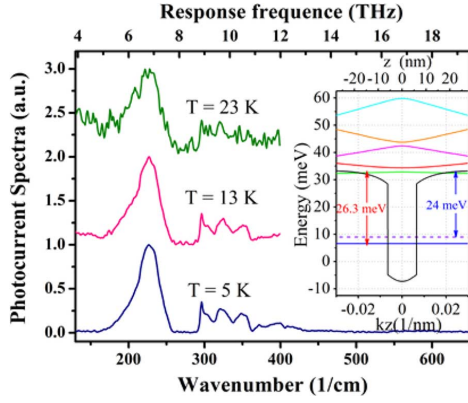


Fig. 4. FTIR response of the test sample at different temperatures, FOV is 90° . The inset depicts the band structure of the sample.

energy from the lowest subband to the first excited subband is 26.3 meV. Further including dynamical many-particle effects, namely depolarization, the calculated peak response is 27.5 meV which is in good agreement with the measured 28 meV considering the uncertainty in the aluminum fraction and the well width during the wafer growth process. Theoretically the activation energy is $V_b - E_1 + E_{ex-co} - E_F = 24$ meV, which is in reasonable agreement but slightly larger than the value of 22.6 meV deduced from the measured dark current shown in Fig. 3(c). The small difference indicates that there may be extra leakage currents due to the very low aluminum fraction used, and perhaps random alloy fluctuations in the very low aluminum regime results in a non-uniform barrier.

D. Performance

In this section, we investigate the key parameters that determine the performance of the detection unit (THz QWP combined with THz QCL) including the signal power density required for PLIP (P_{PLIP}), detectivity (D^*) and the signal to noise ratio (SNR) and point out the directions for possible improvement.

Equating (12) and (13), the required power for PLIP P_{PLIP} for different temperatures can be obtained by

$$P_{PLIP} = \frac{\hbar\nu_p}{\eta^{(1)}\tau_{scatt}} N_2 D A \quad (17)$$

where $\eta^{(1)} = \eta/N_{QW}$ is the absorption efficiency per QW.

Fig. 5(a) illustrates the relation between the minimum signal power density required for PLIP regime and operation temperatures. Once the signal power from the source equals P_{PLIP} , the noise caused by dark current will equal the noise produced by signal illumination and the PLIP condition is reached. The PLIP detectivity can be expressed as

$$D_{PLIP}^* = \frac{\eta^{(1)}}{2\sqrt{2}\hbar\nu_p} \sqrt{\frac{\tau_{scatt} N_{QW}}{N_2 D}} \quad (18)$$

Fig. 5(b) shows the calculated PLIP detectivity of our test sample at different PLIP temperatures. When working at 77 K, the PLIP detectivity obtained is 1.39×10^7 cm \cdot Hz $^{1/2}$ /W. When reaching PLIP, we usually continue to increase the signal power density to reach even better SNR practically. Therefore, SNR is

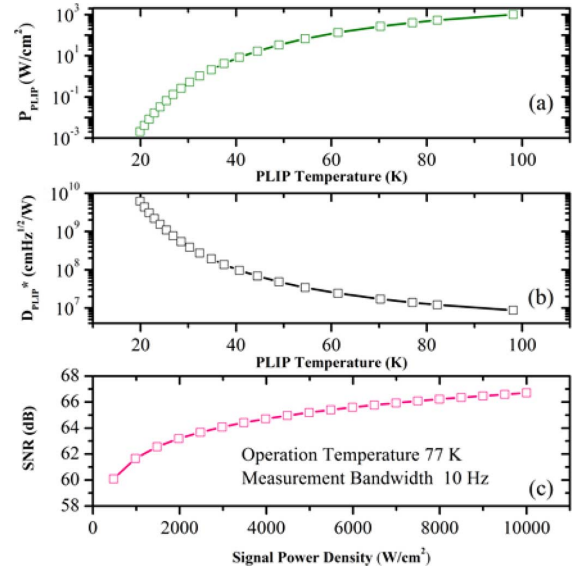


Fig. 5. Calculated (a) required power for PLIP P_{PLIP} and (b) PLIP detectivity D_{PLIP}^* for test sample at different PLIP temperatures. (c) Calculated signal to noise ratio SNR for increased signal power density at 77 K. Measurement bandwidth is set to 10 Hz.

preferred to describe the detector performance and is given by (15). For higher SNR in PLIP regime at fixed temperature, the signal power density should be increased until the dark current can be ignored with respect to the signal current. In this case, the SNR can be simplified to

$$SNR = \sqrt{\frac{P_S \eta^{(1)} N_{QW} A}{4\hbar\nu_p \Delta f}}. \quad (19)$$

Fig. 5(c) gives the calculated SNR versus the signal power density when the sample is operated in the PLIP regime at 77 K. In this calculation, the measurement bandwidth is set as 10 Hz. As shown, applying higher signal power density is an effective way to increase SNR.

IV. DESIGN IMPROVEMENT

In the standard theory of QWP, the generally accepted optimum design is to ensure that the first excited state is in resonance with the top of the barrier. This configuration ensures both large peak absorption and rapid escape of excited electrons at the same time. Also, the barriers should be thick enough such that interwell tunneling is negligible with respect to the current flowing through the device.

To design an optimum QWP, we need to choose the following parameters: well width L_w , Al fraction Al_x , the doping density N_{2Ddope} , barrier width L_b and the number of the wells N_{QW} . Detailed research on THz QWPs design has been conducted by Guo *et al.* [7] and Zhang *et al.* [12]. However, all the parameters chosen are focused on the best performance for THz QWPs working in BLIP regime in the temperature range from 10 to 20 K. For high-temperature detection such as in the PLIP regime, these parameters will not be the optimized ones anymore. It is well known that the QW shape and the confined state energy are determined by three parameters (L_w , Al_x , N_{2Ddope}).

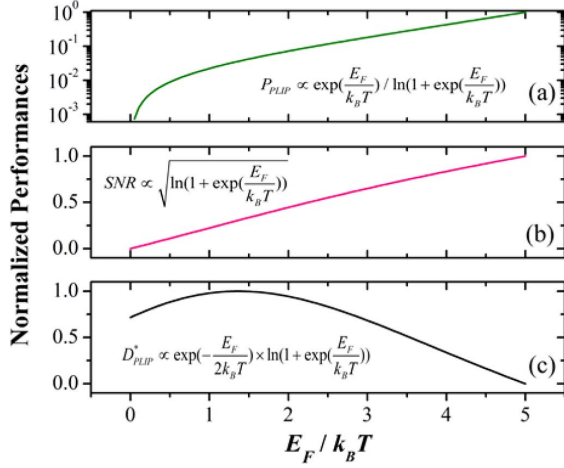


Fig. 6. Relation of (a) required power for PLIP (P_{PLIP}), (b) signal to noise ratio (SNR) and (c) PLIP detectivity (D_{PLIP}^*) as the function of $E_F/k_B T$. All results are normalized.

According to the design rule, the three parameters are not independent, but coupled to each other to ensure that the first excited state is in resonance with the top of the barrier for THz QWPs with fixed frequency. However, there are still many sets of parameters ($L_w, Al_x, N_{2\text{Ddope}}$) that meet the requirement above. So, how to choose the best set of parameters that not only meet the design rule, but also yield better performance? A key step is to fix the doping density $N_{2\text{Ddope}}$ because of its significant effect on the QWP parameters including Fermi energy, absorption efficiency and dark current as well as the potential correction caused by many-particle effects. Increasing the doping concentration $N_{2\text{Ddope}}$, on the one hand, will result in an enhanced absorption efficiency and signal current. On the other hand, many-particle effects will become stronger and eigenenergies fall more deeply. To satisfy this design rule, the aluminum fraction has to be decreased, which will result in an exponential increase of dark current. So there is a dilemma in the selection of doping concentration: weighing the benefits of improving photocurrent against the unwanted enhancement of dark current.

Back to (17)–(19), the expressions for the three key factors (i.e., required power density P_{PLIP} for PLIP operation, PLIP detectivity D_{PLIP}^* , and signal-to-noise ratio (SNR)) can be simplified to

$$P_{\text{PLIP}} \propto \exp\left(\frac{E_F}{k_B T}\right) / \ln\left(1 + \exp\left(\frac{E_F}{k_B T}\right)\right) \quad (20a)$$

$$\text{SNR} \propto \sqrt{\ln\left(1 + \exp\left(\frac{E_F}{k_B T}\right)\right)} \quad (20b)$$

$$D_{\text{PLIP}}^* \propto \exp\left(-\frac{E_F}{2k_B T}\right) \times \ln\left(1 + \exp\left(\frac{E_F}{k_B T}\right)\right). \quad (20c)$$

Fig. 6 illustrates the relation of P_{PLIP} , D_{PLIP}^* and SNR with $E_F/k_B T$. As shown, there is a trade-off between P_{PLIP} and SNR. Reducing $E_F/k_B T$ is an efficient way to obtain low P_{PLIP} , but this will also degrade the SNR. For PLIP detectivity, D_{PLIP}^* increases with $E_F/k_B T$, then peaks at $E_F = 1.37 k_B T$ and decreases as $E_F/k_B T$ increases further.

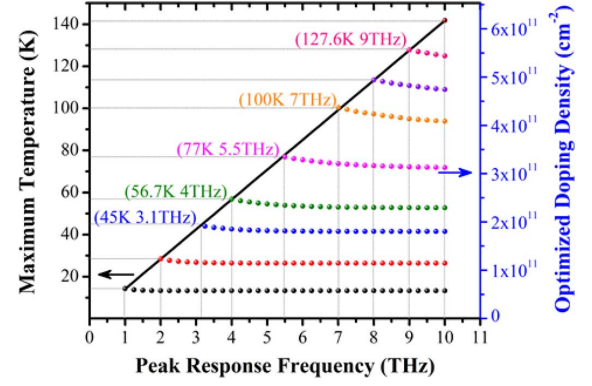


Fig. 7. Optimized doping densities for PLIP performance at various temperatures. The black line indicates the maximum temperatures for THz QWPs with different peak response frequencies.

So, if $E_F = 1.37 k_B T$, we obtain the highest D_{PLIP}^* and relatively lower power density for PLIP (as P_{PLIP} is less sensitive in the region of low $E_F/k_B T$, there is no need to further decrease $E_F/k_B T$ at the expense of decreasing D_{PLIP}^* and SNR). Even though SNR is not high enough, we can also make it higher by increasing the signal power density if higher SNR is preferred at fixed PLIP temperature. Inserting $E_F = 1.37 k_B T$ into (2), we obtain the optimum doping concentration for a given operation temperature.

The bullets shown in Fig. 7 are the calculated optimized doping density for different THz QWPs at various operation temperatures. The black line indicates the maximum temperatures for THz QWPs with different peaks, which are obtained by the assumption that the electrons above the barriers should be less than a certain percentage (we set 15% here) of the total electrons to make sure there are enough confined electrons in the ground state to generate photocurrent. As shown, the maximum temperature grows almost linearly with detection frequency. The optimized doping densities obtained by (2) for different temperatures and detection frequencies are shown with bullets. When the operation temperature is 14.2 K, all QWPs from 1 to 10 THz are functional and the optimized doping densities for all QWPs are almost identical. The value of doping concentration $6 \times 10^{16} \text{cm}^{-3}$, is consistent with the THz QWPs proposed experimentally [17]. When the temperature is increased to 77 K, a lot of electrons originally confined in the ground state escape above the barrier especially in the QWPs with relatively small intersubband energies. To compensate for the escaped electrons, additional Si should be doped to make the electrons on bound state comply with $E_F = 1.37 k_B T$. Thus, at fixed operation temperature, the total doping densities show an increased trend as the peak wavelength grows. Based on the definition of maximum temperatures, only QWPs with peaks at 5.5 THz and above can be operated at 77 K.

Fig. 8 gives the calculated QW widths and aluminum fractions for different response frequencies with optimum doping concentration at 10, 45, 77 and 100 K, respectively. These parameters ($L_w, Al_x, N_{2\text{Ddope}}$) calculated for 10 K are the most common parameters designed for THz QWPs. These parameters are optimized for 10 K, but are no longer optimal at higher temperature. Here, we give 45, 77, and 100 K which starts from

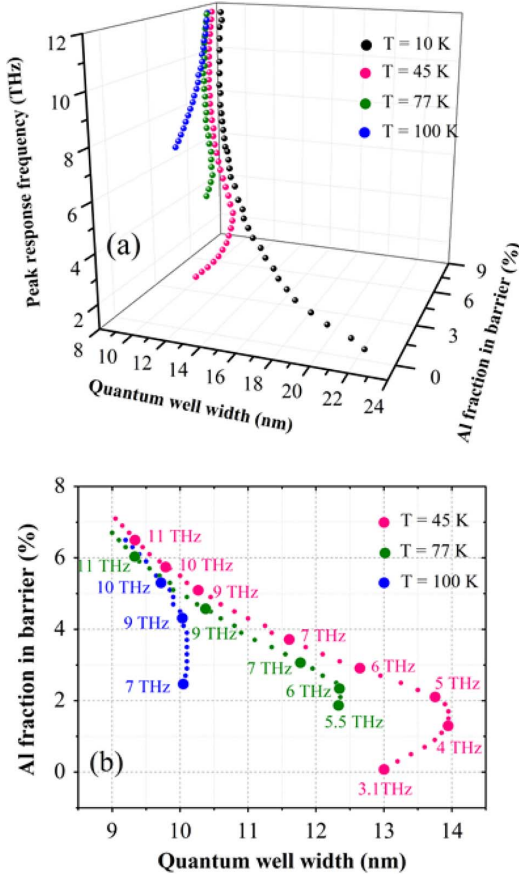


Fig. 8. (a) Calculated QW width and Al fraction for given response peaks at 10, 45, 77 and 100 K. The doping concentration is optimum designed as shown in Fig. 7. The number of periods is 30. (b) Two-dimensional plot. We have included Hartree potential, exchange-correlation and depolarization shift in the calculation.

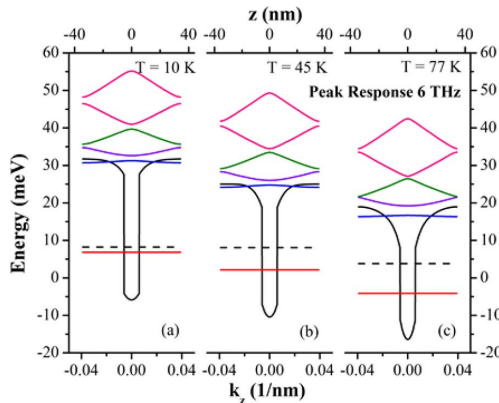


Fig. 9. Band structures of optimal designed THz QWPs with the same peak response 6 THz at (a) 10 K, (b) 45 K and (c) 77 K. The dashed lines are the Fermi levels. The optimal structure parameters are chosen from Fig. 8.

3.1, 5.5 and 7 THz respectively as an example. Clearly, though the target frequency is the same, the set of three design parameters are strongly different at different operation temperature.

Fig. 9 shows the band structures of three optimally designed THz QWPs with the same peak response 6 THz at 10 K, 45 K, and 77 K, respectively. The black lines indicate the band diagrams, color lines are the ground subband plus five minibands

TABLE I
STRUCTURE PARAMETERS OF OPTIMAL DESIGNED 6 THz QWPs AT 10 K, 45 K, AND 77 K

Sample	1#	2#	3#
L_w (nm)	12.4	12.6	12.4
L_b (nm)	62	63	61.8
Al_x (%)	3.8	2.9	2.3
N_{2Ddope} (cm $^{-2}$)	4.27×10^{10}	1.92×10^{11}	3.29×10^{11}
N_{QW}	30	30	30
v_p (THz)	6.0	6.0	6.0
T (K)	10	45	77

L_b is the barrier width, usually taken five times the length of well width L_w to suppress the intertunneling process.

and the dashed lines are the Fermi levels. Detailed designed parameters are illustrated in Table I. As shown, the optimal doping concentration increases with the desired operation temperature and as a result, the influence of many-particle effects on the band structures becomes more prominent. When operated below 10 K, the QWP device of Fig. 9(a) is automatically in the BLIP regime (i.e., one special case of PLIP where the signal is the 300 K background). For fixed operation temperature, it should be noted that in the high-frequency region, the trend of the changing of design parameters are in accordance with the previously proposed design rules [12], [16]. Generally, if a design for lower-frequency QWPs is needed, we could decrease the Al fraction and increase the width of QW simultaneously. However, in the low-frequency region, something different occurs. Lowering the Al fraction will result in an exponentially increasing escape probability of electrons originally confined in QWs, especially at low Al fractions. Thus, many-particle effects become much weaker and eigenenergies fall less deeply. The QW width should be adjusted and even decreased to obtain the target detection frequency and ensure the second subband to be resonant with the top of the barrier.

To indicate their PLIP performances, the required power for THz QWPs to realize PLIP detection is given in Fig. 10(a). The black line represents the corresponding power density when operated at the maximum temperatures. As shown, the required power densities grow rapidly as the detection wavelength and PLIP temperature increase, indicating that the PLIP operation condition is more demanding at lower THz frequencies and higher temperature, which is mainly caused by the higher dark current generated in these parameter regimes. The required power densities can easily be obtained by a high power laser (such as THz QCL), since THz QCL can provide high power up to hundreds of milliwatts. Note that presently THz QCLs still need cooling, which makes them compatible with the operation of THz QWPs. Thus, the combined operation of THz QWP and QCL for gas sensing and other applications is practical. For instance, to realize PLIP detection at 77 K, the frequency of THz QWPs should be no less than 5.5 THz. Taking 5.5 THz QWPs as an example, it needs a signal power higher than 819 W/cm 2 to achieve PLIP, which is far less than the tolerable illumination density 10000 W/cm 2 reported by Liu *et al.* on a $10 \times 10 \mu\text{m}^2$ QWP device [34]. The PLIP detectivity and minimum signal to noise ratio for THz QWPs are also presented in Figs. 10(b) and (c), respectively. Both are obtained

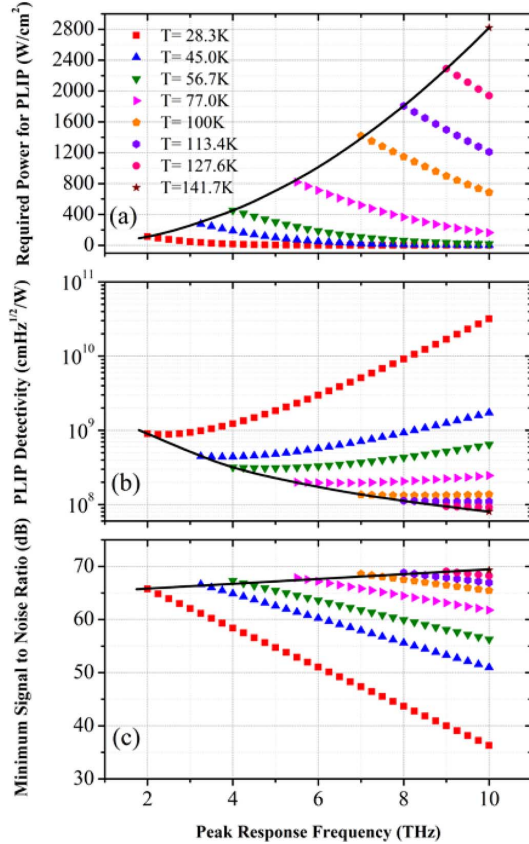


Fig. 10. Calculated (a) required power for PLIP (P_{PLIP}), (b) PLIP detectivity (D_{PLIP}^*) and (c) signal to noise ratio (SNR) as the function of response frequencies at different PLIP temperatures. The THz QWPs' parameters are optimum designed in Fig. 8. The black lines in (a), (b) and (c) represent the corresponding power density, detectivity and signal to noise ratio for each QWP when works at its maximum temperature.

when the QWPs are illuminated with required power to achieve PLIP. Thus, the PLIP detectivity is the maximum while the signal to noise ratio is the minimum. When the signal power density increases at fixed temperature, on the one hand, signal current will be enhanced and better signal to noise ratio will be obtained. On the other hand, the enhanced signal current will result in an increased signal noise current which will inevitably deteriorates the detectivity. Thus, the signal power density could be adjusted as needed for operation.

V. CONCLUSION

In conclusion, we have reported a systematic theoretical and experimental investigation on the PLIP performances of THz QWPs, which could be used in combination with a THz laser for detection at high operation temperature, by analyzing its dark current performance and photocurrent response. We also give the optimal doping concentration for different operating temperature considering its influences on required signal power density for PLIP, detectivity and signal to noise ratio. Accordingly, unlike in previous studies, the optimum doping concentration is not fixed, but determined by the operation temperature. We present optimized designs of THz QWPs for different PLIP temperatures and specify their PLIP performances. Simulated results indicate that a QWP with peak response frequency of

5.5 THz is expected to achieve PLIP at signal power density of 819 W/cm² and above. Higher temperatures (e.g., even higher than 100 K, but below their maximum temperatures) can also be obtained by high-frequency THz QWPs under practical illumination density. In our calculations, many-particle effects have been taken into consideration.

ACKNOWLEDGMENT

The authors are deeply indebted to Prof. H. C. Liu (Fellow, IEEE) who suddenly passed away in October, 2013. This work is also a memory to him.

REFERENCES

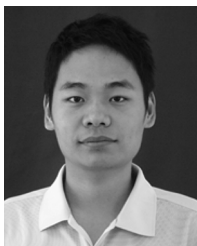
- [1] B. S. Williams, "Terahertz quantum-cascade lasers," *Nat. Photon.*, vol. 1, pp. 517–525, Sep. 2007.
- [2] S. Fatholouloumi *et al.*, "Terahertz quantum cascade lasers operating up to ~ 200 K with optimized oscillator strength and improved injection tunneling," *Opt. Express*, vol. 20, pp. 3866–3876, Feb. 2012.
- [3] J. R. Freeman *et al.*, "Broad gain in a bound-to-continuum quantum cascade laser with heterogeneous active region," *Appl. Phys. Lett.*, vol. 99, p. 241108, Dec. 2011.
- [4] M. Brandstetter *et al.*, "High power terahertz quantum cascade lasers with symmetric wafer bonded active regions," *Appl. Phys. Lett.*, vol. 103, p. 171113, Oct. 2013.
- [5] S. Kumar, "Recent progress in terahertz quantum cascade laser," *IEEE J. Sel. Topics Quantum Electron.*, vol. 17, no. 1, pp. 38–47, Feb. 2011.
- [6] P. Dean *et al.*, "Terahertz imaging using quantum cascade lasers—A review of systems and applications," *J. Phys. D: Appl. Phys.*, vol. 47, p. 374008, July 2014.
- [7] X. G. Guo, J. C. Cao, R. Zhang, Z. Y. Tan, and H. C. Liu, "Recent progress in terahertz quantum-well photodetectors," *IEEE J. Sel. Topics Quantum Electron.*, vol. 19, no. 1, p. 8500508, Feb. 2013.
- [8] S. Nadar *et al.*, "Room temperature imaging at 1.63 and 2.54 THz with field effect transistor detectors," *J. Appl. Phys.*, vol. 108, p. 054508, Jun. 2010.
- [9] M. Bauer *et al.*, "Antenna-coupled field-effect transistors for multi-spectral terahertz imaging up to 4.25 THz," *Opt. Express*, vol. 22, pp. 19250–19256, Jul. 2014.
- [10] H. Schneider and H. C. Liu, *Quantum Well Infrared Photodetectors—Physics and Applications*. Berlin, Germany: Springer-Verlag, 2007, vol. 126, Springer Series in Optical Sciences.
- [11] H. C. Liu, H. Luo, C. Y. Song, Z. R. Wasilewski, A. J. S. Thorpe, and J. C. Cao, "Design of terahertz quantum well photodetectors," *Infrared Phys. Technol.*, vol. 50, pp. 191–193, Nov. 2007.
- [12] S. Zhang *et al.*, "Terahertz quantum-well photodetectors: Design, performance, and improvements," *J. Appl. Phys.*, vol. 114, p. 194507, Nov. 2013.
- [13] H. Schneider, H. C. Liu, S. Winnerl, C. Y. Song, M. Walther, and M. Helm, "Terahertz two-photon quantum well infrared photodetector," *Opt. Express*, vol. 17, pp. 12279–12284, Jul. 2009.
- [14] J. Y. Jia *et al.*, "Dark current mechanism of terahertz quantum-well photodetectors," *J. Appl. Phys.*, vol. 116, Oct. 2014, Art no. 154501.
- [15] M. Graf *et al.*, "Terahertz range quantum well infrared photodetector," *Appl. Phys. Lett.*, vol. 84, p. 475, Nov. 2004.
- [16] H. C. Liu, C. Y. Song, A. J. SpringThorpe, and J. C. Cao, "Terahertz quantum-well photodetector," *Appl. Phys. Lett.*, vol. 84, p. 4068, May 2004.
- [17] H. Luo, H. C. Liu, C. Y. Song, and Z. R. Wasilewski, "Background-limited terahertz quantum-well photodetector," *Appl. Phys. Lett.*, vol. 86, Jun. 2005, Art no. 231103.
- [18] M. Graf *et al.*, "Terahertz quantum well infrared detectors," *Infrared Phys. Technol.*, vol. 52, pp. 289–293, June 2009.
- [19] X. G. Guo, Z. Y. Tan, J. C. Cao, and H. C. Liu, "Many-body effects on terahertz quantum well detectors," *Appl. Phys. Lett.*, vol. 94, May 2009, Art no. 201101.
- [20] J. Zhang and W. Pötzt, "Exchange-correlation effects in resonant-tunneling heterostructure," *Phys. Rev. B.*, vol. 42, no. 17, pp. 11366–11369, Dec. 1990.
- [21] O. Gunnarsson and B. Lundqvist, "Exchange and correlation in atoms, molecules, and solids by the spin-density-functional formalism," *Phys. Rev. B.*, vol. 13, no. 10, pp. 4274–4298, May 1976.
- [22] B. F. Levine, "Quantum-well infrared photodetectors," *J. Appl. Phys.*, vol. 74, p. R1, Jul. 1993.

- [23] M. Ershov, H. C. Liu, M. Buchanan, Z. R. Wasilewski, and V. Ryzhii, "Photoconductivity nonlinearity at high excitation power in quantum well infrared photodetectors," *Appl. Phys. Lett.*, vol. 70, p. 414, Nov. 1997.
- [24] C. Mermelstein, H. Schneider, A. Sa'ar, C. Schönbein, M. Walther, and G. Bihlmann, "Low-power photocurrent nonlinearity in quantum well infrared detectors," *Appl. Phys. Lett.*, vol. 71, p. 2011, Aug. 1997.
- [25] J. Y. Duboz *et al.*, "Electron relaxation time measurements in GaAs/AlGaAs quantum wells: Intersubband absorption saturation by a free-electron laser," *J. Appl. Phys.*, vol. 77, p. 6492, Feb. 1995.
- [26] J. Y. Duboz, E. Costard, J. Nagle, J. M. Berset, J. M. Ortega, and J. M. Gérard, "Electron capture time measurements in GaAs/AlGaAs quantum-well infrared photodetectors: Photoresponse saturation by a free-electron laser," *J. Appl. Phys.*, vol. 78, p. 1224, Mar. 1995.
- [27] X. G. Guo, L. L. Gu, M. Dong, J. C. Cao, H. C. Liu, and F. M. Guo, "Negative differential resistance induced by thermalization of two-dimensional electrons in terahertz quantum-well photodetectors," *J. Appl. Phys.*, vol. 113, p. 203109, May 2013.
- [28] E. Rosencher, F. Luc, P. Bois, and S. Delaire, "Injection mechanism at contacts in a quantum-well intersubband infrared detector," *Appl. Phys. Lett.*, vol. 61, p. 468, May 1992.
- [29] H. C. Liu, "Noise gain and operating temperature of quantum well infrared photodetectors," *Appl. Phys. Lett.*, vol. 61, p. 2703, Sept. 1992.
- [30] H. Schneider, C. Schönbein, M. Walther, P. Koidl, and G. Weimann, "Influence of optical interference on quantum well infrared photodetectors in a 45° waveguide geometry," *Appl. Phys. Lett.*, vol. 74, p. 16, Nov. 1998.
- [31] R. Zhang, Z. L. Fu, L. L. Gu, X. G. Guo, and J. C. Cao, "Terahertz quantum well photodetectors with reflection-grating couplers," *Appl. Phys. Lett.*, vol. 105, p. 231123, Dec. 2014.
- [32] A. Gomez, V. Berger, N. Péré-Laperne, and L.-A. De Vaultier, "Barrier breakdown in multiple quantum well structure," *Appl. Phys. Lett.*, vol. 92, May 2008, Art no 202110.
- [33] A. Delga *et al.*, "Space charge mediated negative differential resistance in terahertz quantum well detectors," *J. Appl. Phys.*, vol. 110, Jul. 2011, Art no 013714.
- [34] H. C. Liu *et al.*, "High absorption (>90%) quantum-well infrared photodetectors," *Appl. Phys. Lett.*, vol. 79, p. 4237, Oct. 2001.



J. Y. Jia was born in Suqian, Jiangsu province, China, on November 2, 1989. He received the B.S. degree in physics from Northeastern University, China, in 2012, and is currently working toward the Ph.D. degree from the Department of Physics and Astronomy, Shanghai Jiao Tong University, China.

His main research interests are related to optical detectors of semiconductor and terahertz technology.



T. M. Wang was born in Baoding, Hebei Province, China, on January 2, 1990. He received the B.S. degree in physics from Shanghai Jiao Tong University, Shanghai, China, in 2012, where he is currently working toward the Ph.D. degree.

His main research interests are related to semiconductor device physics and terahertz technology.



Y. H. Zhang was born in Taizhou, Jiangsu Province, China. She received her Ph.D. degree in Tongji University in 2001.

She joined the Shanghai Jiao Tong University as post doctorate in 2001. She is currently an Associate Professor in the Department of Physics and Astronomy of Shanghai Jiao Tong University, Shanghai, China. Her main research interest is semiconductor quantum devices.



W. Z. Shen was born in Suzhou, Jiangsu Province, China, on May 22, 1968. He received the Ph.D. degree in semiconductor physics and semiconductor device from Shanghai Institute of Technical Physics, Chinese Academy of Sciences, China, in 1995.

From 1995 to 1996, he worked as an assistant professor in National Laboratory for Infrared Physics, Shanghai Institute of Technical Physics. From 1996 to 1999, he was a research associate in Department of Physics and Astronomy, Georgia State University, USA. Since 1999, Dr. Shen has been with Shanghai Jiao Tong University, China, as a full professor in the Department of Physics. Since 2009, he also holds the position of the director of Key Laboratory of Artificial Structures and Quantum Control, Ministry of Education. His main research interests are in the fields of optical and electrical properties of semiconductors, as well as semiconductor quantum electronic devices. He has authored and co-authored more than 200 papers, 3 book chapters, and granted 18 patents.

Prof. Shen was granted the Chinese Distinguished Young Scientist Award in 2001, the Changjiang chair professor of National Minister of Education at Shanghai Jiao Tong University during 2000–2005, and the leader of Changjiang innovation group of National Minister of Education during 2005–2008.



H. Schneider received the Diplomas (M.Sc.) in physics and in mathematics from the University of Tübingen, Germany, in 1985, and the Ph.D. degree from the Max-Planck Institute for Solid State Research, Stuttgart, Germany, in 1988.

From 1989 to 2005, he was with the Fraunhofer Institute for Applied Solid State Physics, Freiburg, Germany. Since 2005 he has been a department head at the Helmholtz-Zentrum Dresden-Rossendorf, Dresden, Germany. His current research interests include electrical and optical properties of solids, in

particular semiconductor quantum structures for infrared and THz optoelectronics.

Dr. Schneider is a member of the German Physical Society (DPG). In 1988, he was a recipient of the Otto-Hahn-Medal (awarded for the best Ph.D. theses of the Max-Planck-Society). In 2001, he received the Science Award issued by the German Science Foundation.